

FINITE ELEMENT STUDY ON PINNING RETROFITTING TECHNIQUE OF MASONRY WALLS WITH OPENING SUBJECTED TO IN-PLANE SHEAR LOAD

Kshitij C. SHRESTHA ^a, Takuya NAGAE ^b, Yoshikazu ARAKI ^{c*}

^a MSc, PhD Student; Department of Architecture and Architectural Engineering, Graduate School of Engineering, Kyoto University, Katsura, Nishikyo, Kyoto 615-8540, Japan

^b Senior Researcher; E-Defense, National Research Institute for Earth Science and Disaster Prevention, Shinjimicho, Miki, Hyogo, 673-0151, Japan

^c Associate Prof.; Department of Architecture and Architectural Engineering, Graduate School of Engineering, Kyoto University, Katsura, Nishikyo, Kyoto 615-8540, Japan

*E-mail address: araki@archi.kyoto-u.ac.jp

Received: 5.09.2011; Revised: 7.11.2011; Accepted: 15.12.2011

Abstract

The paper focuses on finite element (FE) modelling of in-plane response of retrofitted masonry walls when subjected to quasi-static in-plane cyclic loading. The retrofit technique involves inserting inclined and horizontal stainless steel bars, already practiced in several historical masonry constructions in Japan. The strength of the pinning technique is ease of construction and it maintains the original appearance of the URM walls. This paper presents a 2D FE model for the retrofitted masonry walls, where continuum elements represent brick units, interface elements represent brick unit/mortar interface, and truss elements represent reinforcing bars. FE model with the proposed simplified equivalent vertical bar model, to represent the inclined inserted reinforcing bars, is validated by comparisons with the experimental results. It was found from the experimental and numerical results that retrofitted specimens showed substantial increment in both strength and ductility and showcased the applicability of the pinning retrofitting technique for historical masonry constructions.

Streszczenie

W artykule skoncentrowano się na modelowaniu elementami skończonymi naprawionych ścian murowych poddanych quasi statycznemu, płaskiemu obciążeniu cyklicznemu. Technika naprawy, zastosowana w Japonii w różnych obiektach historycznych o konstrukcji murowej, wymaga wkładania ukośnych i poziomych nierdzewnych prętów stalowych. Zaletą takiej techniki kołkowania jest łatwość wykonania oraz zachowanie niezmienionego wyglądu ścian bez zbrojenia. W artykule przedstawiono dwuwymiarowy model elementów skończonych dla naprawianych ścian murowych, gdzie elementy ciągłe przedstawiają poszczególne cegły, elementy kontaktowe odwzorowują powierzchnię styku cegły i zaprawy, a elementy kratownicowe przedstawiają pręty zbrojenia. Model elementów skończonych z zaproponowanym uproszczeniem zastąpienia prętów ukośnych elementami pionowymi został zweryfikowany przez porównanie z wynikami badań doświadczalnych. Na podstawie wyników badań doświadczalnych i numerycznych stwierdzono, że naprawione elementy wykazują znaczący wzrost wytrzymałości i plastyczności, co potwierdza możliwość stosowania tej metody naprawy w historycznych obiektach o konstrukcji murowej.

Keywords: Masonry; Pinning retrofit technique; In-plane shear load; Finite element modelling; Performance assessment.

1. INTRODUCTION

Historical masonry constructions show considerable states of degradation due to action of earthquakes and with the advent of time, undergo constant structural

decay and damage [1]. Vulnerability of historical masonry constructions under earthquake excitations has been seen in the very recent Italy earthquake [2]. Thereby, there is a strong need for improving the performance of historical masonry constructions.

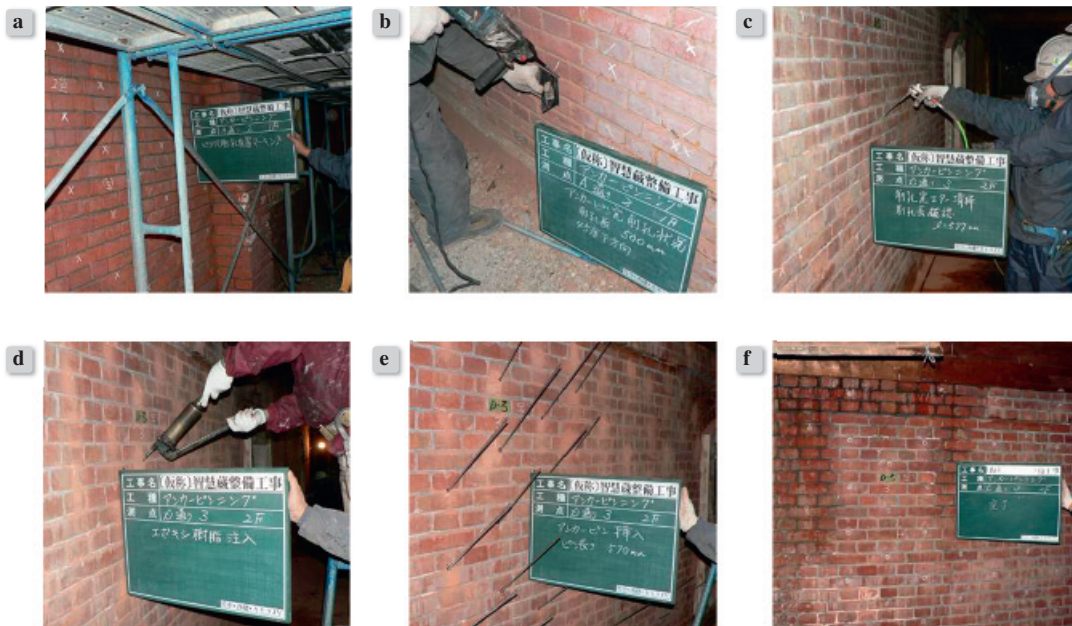


Figure 1.

Pinning retrofitting process: (a) Marking of points for drilling; (b) Drilling at marked points; (c) Air washing of drilled holes; (d) Insertion of epoxy resin; (e) Insertion of pin; (f) Retrofitted wall after pin insertion

Recognizing the shortcomings of unreinforced masonry (URM) walls, there has been a surge of interest in recent years to develop techniques for improving their seismic behaviour. Past research works [3-7] done for improving the seismic performance of URM walls involve: (1) attachment of reinforcing members, (2) surface treatment, (3) grout injection, (4) post-tensioning, and (5) reinforced core technique. The first two techniques usually change the appearance of URM constructions significantly and may cease their aesthetic value, which is problematic especially in retrofitting historical masonry constructions. Although the rest of the techniques do not cause significant changes to the appearance of URM constructions, they have shortcomings. Grout injection does not improve ductility. The other two techniques require removal of roof and changes to existing foundation, which are troublesome from the viewpoints of construction cost and time. Difficulties associated with the preservation of historical masonry constructions, durability of strengthening materials, and also restriction on the parts of a construction to be damaged make the choice of retrofitting technique more challenging.

To overcome the above difficulties, a fairly effective retrofitting technique, where inclined stainless steel bars are inserted into the URM walls, has been applied to several historical brick buildings in Japan [8]. Fig. 1 shows an example of procedure involved in

pinning retrofitting technique. As shown in Figs. 1 (a) to (f), in the retrofitting process, first, points are marked for drilling. Then holes are drilled diagonally followed by air washing of drilled holes. Then epoxy resin is injected for the bonding of reinforcing bars to the masonry elements. And finally steel bars are inserted. The preservation of appearance is attained by inserting steel bars from the mortar joints. The strength of this technique is ease of construction, wherein removal of roof and changes to foundation are unnecessary. This contributes to lower construction cost and shorter construction period. Since the stainless steel bars are inserted from the mortar joints, the retrofit technique maintains the original appearance of the URM wall. Nonetheless, to the authors' knowledge, no numerical modelling has been performed for the masonry walls retrofitted by this technique. The authors have previously reported a finite element (FE) study on pinning retrofitting technique practiced on walls when subjected to out-of-plane loading [9]. The present study focuses on the in-plane shear loading on masonry walls.

This paper develops a simplified 2D FE model for assessing the seismic performance of masonry walls retrofitted by inserting inclined stainless steel bars. In the present model, continuum elements represent brick units, and interface elements with discrete crack approach represent brick unit/mortar interfaces. For reinforced masonry (RM) walls, reinforcing

ing bars are represented by truss elements. For 2D representation of inclined inserted bars, authors have proposed a simplified equivalent vertical bar model, as shown in Fig. 2, where model with cross pinning at 45 degree in Fig. 2(a) is represented by a 2D equivalent vertical bar model in Fig. 2(b). The equivalent vertical bar model facilitates in providing both stability as well as reduction in computation burden as compared to more complex 3D FE model. The proposed FE model is validated by comparisons with the past experimental results [10]. Also theoretical predictions are given for understanding the experimental as well as numerical results from the view point of collapse mechanisms.

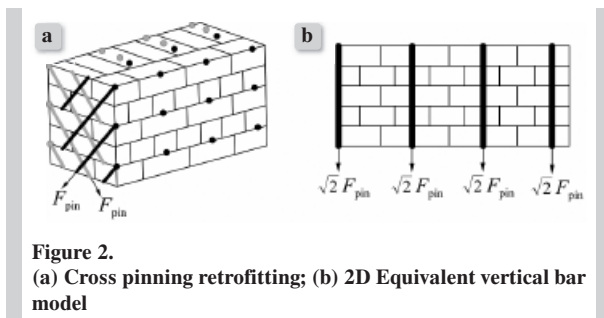


Figure 2. (a) Cross pinning retrofitting; (b) 2D Equivalent vertical bar model

2. FE MODELLING

2.1. Masonry wall specimens

Figs. 3 and 4 show the geometry of the URM and RM specimens respectively. Pinning retrofitting technique involves insertion of inclined stainless steel bars into the brick walls diagonally from the mortar joints in the plane perpendicular to the wall as shown in Fig. 4. Note that the locations of the reinforcing bars inserted from one side of the wall were slightly displaced from those of the reinforcing bars inserted from the other side of the wall as shown in Fig. 4. The circles in the figures indicate the front location from where steel bars are inserted diagonally. Additionally, for RM specimens, reinforcing bars are also inserted in the horizontal direction just above and below the opening on both faces of walls, purely to provide shear resistance and resist diagonal shear cracking of wall. Effectiveness of bed joints structural repointing to enhance the shear resistance of masonry walls have been investigated by numerous previous studies [11-14]. In the present retrofitting technique, the process of insertion involves first removal of mortar along the bed mortar joint level using grinder to make a straight groove 10 mm thick and 10-15 mm deep. This is followed by application of first layer of epoxy resin in the

incision formed. Afterwards reinforcing bar is inserted and finally a second layer of epoxy resin is applied to cover the bar sufficiently. It should be noted that the proposed technique does not show particularly any difficulty in application.

2.2. Masonry wall model

2.2.1. General strategy

Masonry walls, subjected to in-plane shear loading, predominantly undergo tensile and shear failure in mortar joints with very minimal compressive masonry failure. The in-plane response is often governed by cracking at mortar joints and rocking resistance due to gravity. Masonry walls can therefore be represented by simplified interface elements [15] – an approach that does not distinguish failure of the brick-mortar interface from that of the mortar layer itself. Here, a 2D FE model was generated and analyzed using the DIANA9.3 FE program [16], with modelling assuming that brick units are fully elastic and that all material nonlinearity is concentrated on the unit/mortar interface. For reinforced masonry walls, reinforcing bars are represented by truss elements. For 2D representation of inclined inserted bars, authors have introduced the concept of simplified equivalent vertical bar model where inclined inserted bars in a 3D model is replaced by an equivalent vertical bar in a 2D plane as shown in Fig. 2. The proposed 2D FE model is validated by comparisons with the experimental results [10]. Rocking resistance due to gravity is considered by including geometric nonlinearity in the analysis.

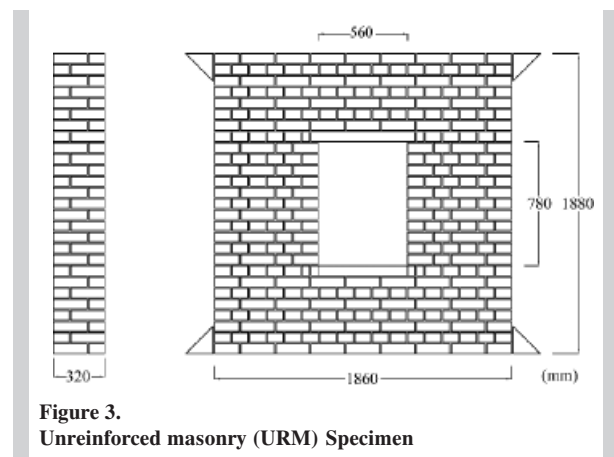


Figure 3. Unreinforced masonry (URM) Specimen

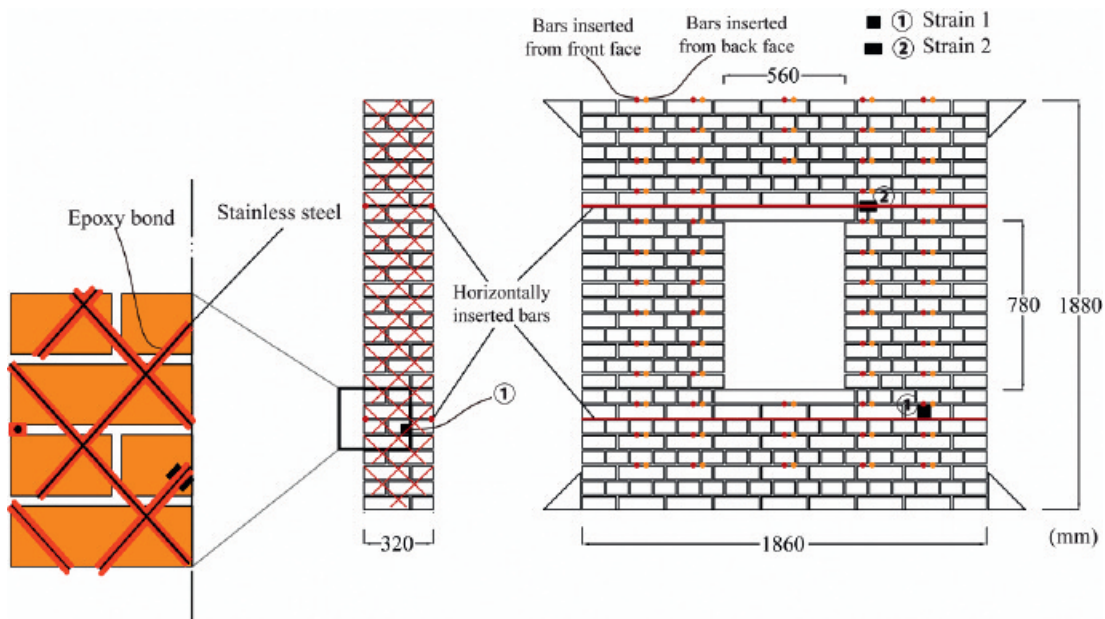


Figure 4.
Reinforced masonry (RM) Specimen

2.2.2. Brick unit model

A masonry brick unit was modelled using rectangular continuum elements connected to vertical and horizontal interface elements. An FE model with meshing for a brick unit is shown in Fig. 5. As stated, brick units were modelled to be perfectly elastic during the whole loading history and modelled with four-node quadrilateral continuum elements. Material properties used include Young's modulus, $E_{\text{brick}} = 20 \text{ GPa}$, Poisson's ratio, $\nu_{\text{brick}} = 0.15$, and density, $\rho_{\text{brick}} = 2000 \text{ kg/m}^3$. These material constants were obtained through compressive tests in masonry prisms and brick units. Additionally, for the potential cracks in the bricks, brick crack interface was also modelled with its location as shown in Fig. 5. A simple discrete cracking model, where a gap arises if tensile traction normal to the interface exceeds tensile strength of 2 MPa, was assumed [15]. It should be noted that we limited the location of brick crack interfaces along the line of mortar joints so as to limit number of elements in FE model. Assignment of zero-thickness interface element meant the length of reinforcing bar between the two corresponding nodes to be zero which is undesirable. For this reason, here brick/mortar interface and brick/crack interface has an actual thickness of 10 mm representing the thickness of mortar joint. As a result, there exists small error in the FE geometry but this has very negligible effect on the final response of specimen.

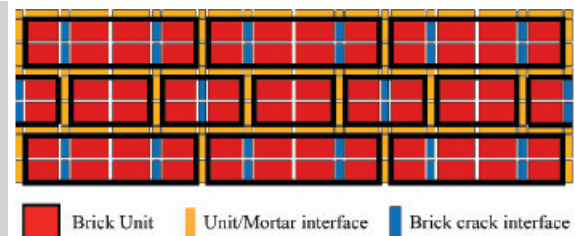


Figure 5.
Masonry unit, unit/mortar interface and brick crack interface discretization (shrunked mesh)

2.2.3. Mortar joint model

An entire mortar joint is represented by a brick unit/mortar interface model implemented in DIANA9.3 [16] as linear interface elements between two lines (2+2 nodes). The constitutive model was a Coulomb friction criterion with tension cut-off. The composition of water, cement, sand and lime for the mortar used was 1:1:6:2. A gap arises if tensile traction normal to the interface exceeds tensile strength of 0.2 MPa. A slip occurs if traction parallel to the interface exceeds shear strength of 0.24 MPa. We obtained tensile strength through bending tests on masonry assemblages [17] and shear strength through shear tests done on masonry triplets [18]. After the gap forms, tensile traction immediately drops to zero, representing brittle cracking.

The model follows classical elastic-plastic formulation:

$$\dot{\mathbf{t}} = \mathbf{D}^e \Delta \dot{\mathbf{u}}^e \quad (1)$$

$\mathbf{t} = \{t_n \ t_t\}^T$, with t_n and t_t normal and shear stress at the interface and \mathbf{D}^e the diagonal matrix with elastic constants D_{11} and D_{22} . Total relative displacement rate $\Delta \dot{\mathbf{u}}$ is assumed to decompose into reversible part $\Delta \dot{\mathbf{u}}^e$ and irreversible part $\Delta \dot{\mathbf{u}}^p$:

$$\Delta \dot{\mathbf{u}} = \Delta \dot{\mathbf{u}}^e + \Delta \dot{\mathbf{u}}^p \quad (2)$$

$\Delta \mathbf{u} = \{\Delta u_n \ \Delta u_t\}$, with Δu_n and Δu_t relative normal and shear displacement across a crack. The following Coulomb friction yield surface models the fracture:

$$\mathbf{f} = \sqrt{t_t^2} + t_n \tan \varphi(\kappa) - \bar{c}(\kappa) = 0 \quad (3)$$

$\tan \varphi(\kappa)$ is the friction coefficient as a function of internal parameter κ and $\bar{c}(\kappa)$ cohesion as a function of internal parameter κ . Internal parameter κ evolution is assumed and given by the irreversible relative displacement component in tangential direction as $\dot{\kappa} = |\Delta \dot{\mathbf{u}}_t^p|$ using the following plastic potential surface:

$$\mathbf{g} = \sqrt{t_t^2} + t_n \tan \psi \quad (4)$$

The direction of irreversible displacement is given by plastic potential function \mathbf{g} . Uplift is determined by dilatancy angle ψ , with $\Delta \dot{\mathbf{u}}^p = \lambda \partial \mathbf{g} / \partial \mathbf{t}$, where λ is the plastic multiplier. Tests on shear triplets [18] determined shear parameters to be $c = 0.24$ MPa and $\tan \varphi = 0.6$. The dilatancy angle is $\tan \psi = 0.6$ [15]. Normal and shear interface joint stiffness are obtained as follows:

$$D_{11} = \frac{E_b E_m}{t_m (E_b - E_m)}, \quad D_{22} = \frac{G_b G_m}{t_m (G_b - G_m)} \quad (5)$$

t_m is mortar joint thickness, E_b and E_m are Young's modulus of the brick unit and mortar, and G_b and G_m are their shear moduli [15]. For this purpose, compressive test on masonry assemblage was done for the determination of Young's modulus of elasticity of brick units ($E_b = 59.5$ GPa) and masonry assemblages ($E_{\text{masonry}} = 1987$ MPa). The elastic modulus of mortar was then assumed in such a way to reproduce the global elastic modulus of masonry. The average maximum compressive strength of masonry assemblage was obtained to be 10.35 MPa and the Young's modulus of mortar, E_m was computed to be 291 MPa.

Using Eq. (5), normal stiffness $D_{11} = 30$ N/mm³ and shear stiffness $D_{22} = 13$ N/mm³ are used for the unit/mortar interface.

Additionally, two special mortar joints are also included in the modelling. Strong mortar joint just above and below the horizontally inserted reinforcing bar to represent the epoxy resin and weak mortar joint at the interface between the top beam and wall specimen as shown in Fig. 6. Discrete crack model is used, where a gap arises if tensile traction normal to the interface exceeds tensile strength of 4 MPa for strong mortar joint and 0.05 MPa for weak mortar joint.

2.3. Reinforcing bar models

2.3.1. Equivalent vertical bar model

The equivalent vertical bar model facilitates in providing both stability as well as reduction in computation burden as reported by previous study done by authors [9]. Application of similar model for in-plane shear loading condition using an equivalent vertical bar to represent inclined reinforcing bars is shown in Fig. 6. Equivalent vertical bars are shown by thick blue vertical solid lines. Black circles show nodes where truss and continuum elements are connected. Material properties are represented by elastic perfectly plastic properties adopting Young's modulus for steel $E_{st} = 210$ GPa and yield stress $f_y = 600$ MPa. It should be noted that fully threaded stainless steel reinforcing bars (SUS304) were used for retrofitting to provide good bond strength. Material properties adopted for the reinforcing bars are based on tensile tests performed on threaded bars.

To determine the equivalent vertical bar cross-sectional area, we count minimum number n of steel bars at the wall's critical section. As shown in Fig. 4, reinforced specimen has 2 lines of reinforcement, i.e., at least 2 reinforcing bars at any horizontal wall section. Bars are inclined at a $\pi/4$ radian to the vertical axis, so cross-sectional area $A_{\text{bar}}^{\text{eq}}$ of the equivalent vertical bar is computed as $A_{\text{bar}}^{\text{eq}} = n A_{\text{bar}} \cos(\pi/4)$. A_{bar} is the cross-sectional area of each stainless steel bar.

2.3.2. Horizontally inserted bar model

A stainless steel bar is presented by a two-node truss element with material properties represented by elastic perfectly plastic properties adopting Young's modulus for steel $E_{st} = 210$ GPa and yield stress $f_y = 600$ MPa – material constants obtained from ten-

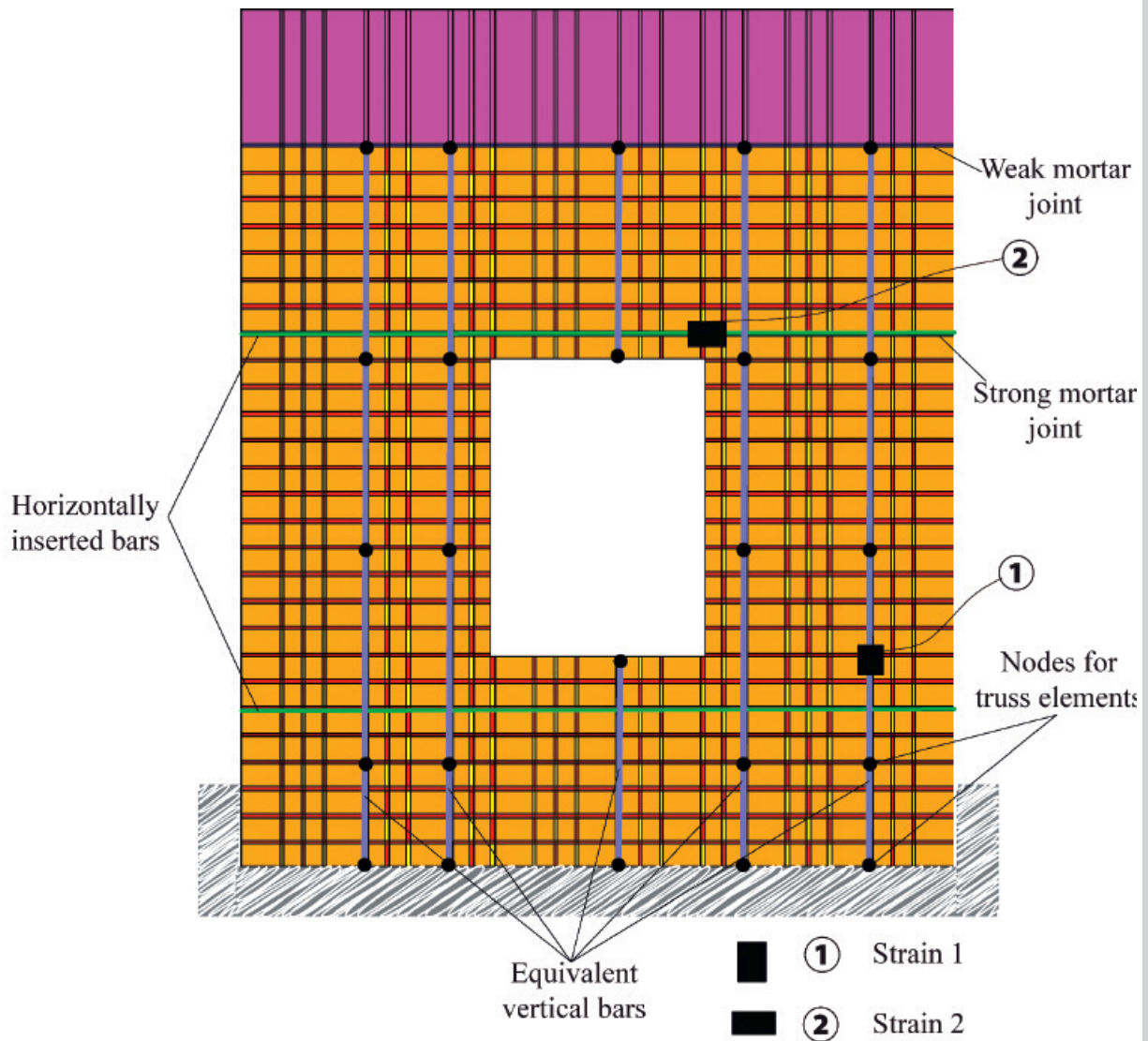


Figure 6.
Finite element (FE) model for RM specimen

sile tests on stainless steel bar specimens 6 mm in diameter. Similar fully threaded stainless steel bars (SUS304) were used as horizontally inserted bars. Green horizontal lines in Fig. 6 represent the horizontally inserted bar in the FE model.

Pull-out tests showed the bond between the reinforcing bar and masonry elements to be stronger than that of the reinforcing bar for minimum bond length of 60 mm which is generally met for the retrofitted specimen as shown in Fig. 4. For this reason, both ends of each truss element were connected to corresponding nodes of continuum elements representing bricks and no relative displacement was allowed between truss element end nodes and corresponding

continuum element nodes. Another important reason for above assumption of perfect bond was to reduce the model complexity and get better solution convergence.

2.4. Loading and boundary conditions

The test setup in Fig. 7 has the in-plane shear load coming at the top section of wall, with constant vertical load of 20 kN at the top. Test arrangement as shown in Fig. 7 does not allow rotation of the top portion of the wall with pure shear realized through shear load acting at the centre of the specimen. This has been simulated in numerical model with a multi point constraint at the top portion of the specimen

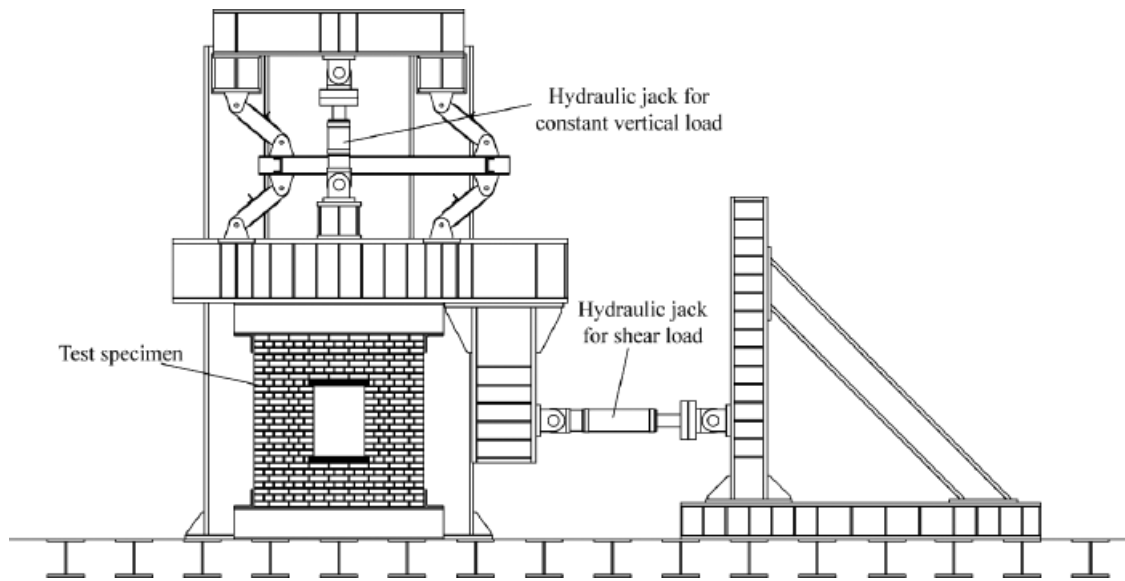


Figure 7.
Experimental test set up

for horizontal and vertical translational motion, restraining the rotation of the top portion of wall, to meet the experimental boundary conditions. A displacement-controlled cyclic load was provided to make maximum rotation angle θ_{\max} of the wall specimen equal to $\pm 1/500, 1/400, 1/200, 1/100, 1/66, 1/50, 1/33$ and $1/20$ radian. The authors have limited presentation of the experimental and numerical results for URM specimen with rotation angle up to $\theta_{\max} < 1/400$ radian and for RM specimen up to $\theta_{\max} < 1/200$ radian only since these small deformation ranges are important for design purposes. Additionally there were also convergence problems during FE analysis at large deformation angle that restricted presentations of numerical simulations up to above mentioned rotation angles. Readers can refer to Appendix section of this paper for full experimental cyclic response for URM and RM specimens.

3. THEORETICAL PREDICTIONS

Collapse capacity of reinforced and unreinforced masonry walls with opening subjected to in-plane shear load can be effectively predicted assuming the failure mechanism with designated plastic locations and computing the rocking resistance based on equilibrium states [19]. Failure mechanism depends on the relative strength of element sections with two extreme cases – (1) Strong pier-weak beam mechanism and (2) Strong beam-weak pier mechanism. Both these mechanisms are illustrated in Figs. 8 and 9.

3.1. Strong pier-weak beam mechanism

From Fig. 8, with strong pier-weak beam failure mechanism, following equilibrium conditions for RM specimen can be obtained from the given free body diagrams:

From free body T*:

$$\begin{aligned} F_R &= F_A^H + F_B^H \\ F_v &= F_A^V + F_B^V \end{aligned} \quad (6)$$

From free body A*:

$$F_A^H h_1 = F_A^V L + H h_2 + w_d L / 2 + F_p (L_{p1} + L_{p2}) \quad (7)$$

From free body B*:

$$F_B^H h_1 = F_B^V L - H h_2 + w_d L / 2 + F_p (L_{p3} + L_{p4}) \quad (8)$$

Solving Eqns. 6, 7 and 8, the capacity of wall is obtained as follows:

$$\begin{aligned} F_R^{\text{RM}} &= \frac{L}{h_1} \left\{ F_v + w_d + F_p \frac{(L_{p1} + L_{p2} + L_{p3} + L_{p4})}{L} \right\} \\ F_R^{\text{URM}} &= \frac{L}{h_1} (F_v + w_d) \end{aligned} \quad (9)$$

Here, we consider the capacity only after diagonal cracking, i.e., contribution of shear strength parameters Q_v and Q_h as shown in Fig. 8 (b) has not been taken into account in the above strength formulation.

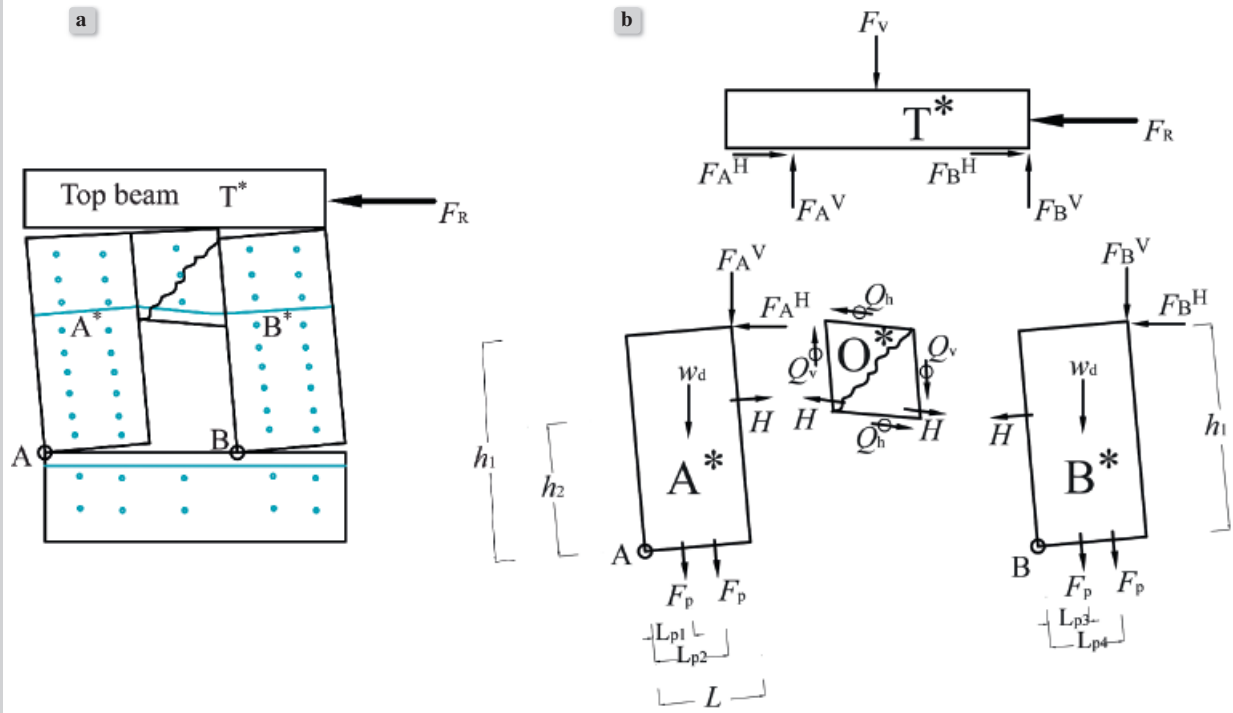


Figure 8. Weak beam-strong pier failure mechanism for RM specimen: (a) Deformed shape; (b) Free body diagrams

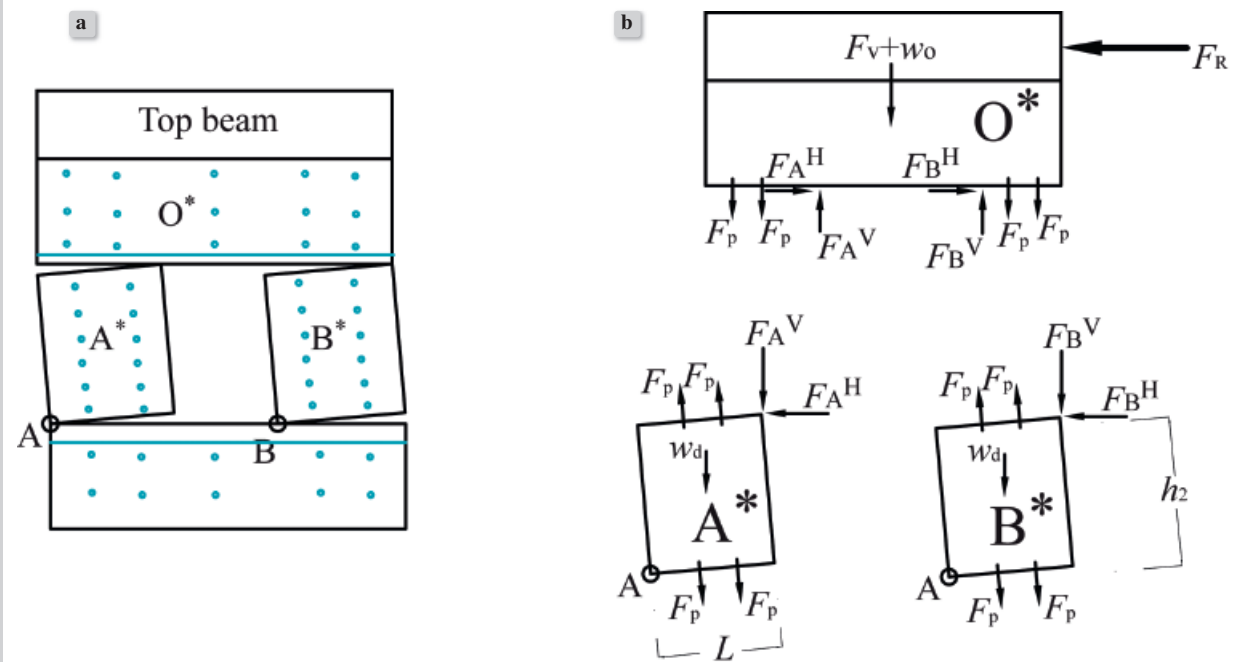


Figure 9. Weak pier-strong beam failure mechanism for RM specimen: (a) Deformed shape; (b) Free body diagrams

3.2. Strong beam-weak pier mechanism

From Fig. 9, with strong beam-weak pier failure mechanism, following equilibrium conditions for RM specimen can be obtained:

From free body O*:

$$\begin{aligned} F_R &= F_A^H + F_B^H \\ F_v + w_0 + 4F_p &= F_A^v + F_B^v \end{aligned} \quad (10)$$

From free body A*:

$$F_A^H h_2 = F_A^v L + w_d L / 2 \quad (11)$$

From free body B*:

$$F_B^H h_2 = F_B^v L + w_d L / 2 \quad (12)$$

Solving Eqns. 10, 11 and 12, the capacity of wall is obtained as follows:

$$\begin{aligned} F_R^{RM} &= \frac{L}{h_2} (F_v + w_0 + w_d + 4F_p) \\ F_R^{URM} &= \frac{L}{h_2} (F_v + w_0 + w_d) \end{aligned} \quad (13)$$

The failure mechanisms and subsequently the resisting force computed using Eqns. 9 and 13 give two extreme upper and lower bound values. However, the actual failure pattern and resisting force observed experimentally is generally between these two cases. Theoretical prediction made on the basis of experimentally observed final failure pattern has been shown in Appendix section of this paper with large deformation results.

4. RESULTS

4.1. URM Specimen

4.1.1. Summary of experimental observations

Experimental cyclic loading history is shown in Fig. 10 where response for maximum rotation angle up to $\theta_{max} < 1/400$ radian is presented. A maximum load of 30.2 kN was observed at the very small rotation angle just before cracking. After cracking was initiated, brittle failure occurred with an almost constant residual force of about 20 kN. Here the pre-cracking response remained almost linear until peak force was observed and post-cracking mode is dominated by the sudden drop in resisting force due to brittle failure. An almost constant resisting force was observed thereafter corresponding to the wall's shear and rocking resistance.

The presence of opening governed the failure mechanism with diagonal shear cracking originating from the extreme edges of opening and finally causing rocking of piers as shown by the dotted lines in Fig. 11 (a).

4.1.2. Comparison with numerical simulation

Comparison is made between experimental and numerical response in Fig. 10 within the small rotation angle up to $\theta_{max} < 1/400$ radian. The numerically computed and experimentally observed resisting forces agree well with each other. Numerical response also shows similar pre-cracking response with almost linear behaviour up to initial peak strength. With the completion of pre-cracking, the specimen in the immediate post-cracking stage shows significant wall deformation with no real increase in resisting force with good agreement between the FE and experimental results. Fig. 11 (b) shows the FE deformed shape for URM specimen at deformation angle of $\theta_{max} = 1/1200$ radian which reflects the instant when maximum horizontal resisting force is observed. The contour of colour in Fig. 11(b) represents the distribution of principal tensile and compressive stresses in FE model.

4.1.3. Comparison with theoretical predictions

Comparisons have been made with two extreme cases – strong pier-weak beam and strong beam-weak pier mechanisms as described previously in Sections 3.1 and 3.2. For strong pier-weak beam mechanism, using

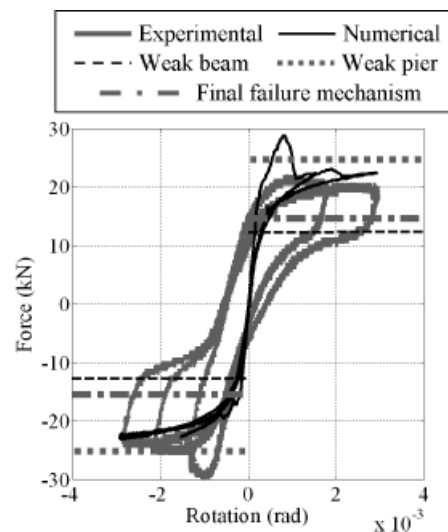


Figure 10. Force deformation comparison for URM specimen for $\theta_{max} < 1/400$ radian

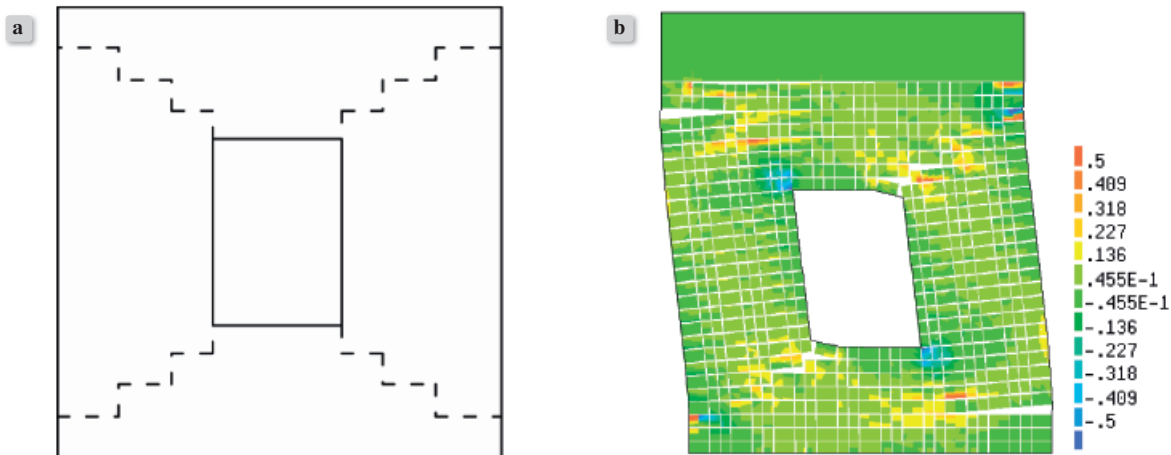


Figure 11. Deformed shapes for URM specimen: (a) Experimentally observed for $\theta_{max} < 1/400$ radian; (b) Numerical simulation for $\theta_{max} < 1/1200$ radian

Eqn. 9 with L ($=650$ mm) the width of pier, h_1 ($=1330$ mm) the height of reaction force from the point of rotation, F_v ($=20$ kN) the vertical load applied at the top of the specimen and w_d ($=5.5$ kN) the weight of pier, horizontal resisting force F_R^{URM} of 12.46 kN is obtained. The mechanism underestimates the resistance offered by masonry wall as shown in Fig. 10.

For strong beam-weak pier mechanism, the resisting force F_R^{URM} of 24.83 kN is obtained from Eqn. 13 which overestimates the experimental response as shown in Fig. 10. Here h_2 ($=780$ mm), w_0 ($=6.55$ kN) and w_d ($=3.25$ kN) are taken for computation. w_0 is the weight of brick wall resting on the rocking pier. Additionally, prediction based on the final failure pattern has also been done with failure pattern and subsequent formulation given in Appendix Section A1. The resisting force computed from final failure mechanism gives value of 14.4 kN which again underestimates the experimental response as shown in Fig. 10. Although the reason for this comparatively lower value of resisting force is unclear, friction is one possible reason.

4.2. RM Specimen

4.2.1. Summary of experimental observations

Fig. 12 (a) shows the relationship of resisting force and the rotation angle for RM specimen for small deformation range of $\theta_{max} < 1/200$ radian. In contrary to URM specimen response, RM specimen showed higher resisting force and ductility without sudden decrement in strength, showing the effectiveness of

reinforcing bars inserted. In addition to force deformation history, strains experienced by the reinforcing bar at two primary locations are shown in Figs. 13 (a) and (b). Fig. 13 (a) shows strain history for the bar inserted at an angle of $\pi/4$ radian perpendicular to the plane of wall shown by Strain 1 in Fig. 4 and Fig. 13 (b) is for horizontally inserted bar; its location represented as Strain 2 in Fig. 4. Note that strain gage history has been plotted for small deformation range of $\theta_{max} < 1/200$ radian, representing the instant when inclined inserted reinforcing bar just started yielding. The strain gage history shows clearly effectiveness of both inclined as well as horizontal inserted bars in providing resistance to shear failure of masonry walls. The failure mechanism observed is shown in Fig. 12(b) with mix failure mechanism explained in section 4.2.2. Diagonal shear failure observed for URM specimen was prevented for RM specimen.

4.2.2. Comparison with numerical simulation

Comparison is made between experimental and numerical response in Fig. 12 (a), in terms of force deformation history within the small rotation angle up to $\theta_{max} < 1/200$ radian. Comparisons between strain gage histories are shown in Figs. 13 (a) and (b). Resisting force observed experimentally was slightly lower as compared to numerically computed value. The reason is complex and mixed failure mechanism observed during experimentation; there was significant damage in masonry at top portion of wall specimen which was not seen in case of numerical simulation. It should be noted that reinforcing bar just started to yield at this deformation range, hence no sig-

nificant energy dissipation in case of numerical results was observed. Good agreements were found for strain gage histories both for Strain 1 as well as Strain 2. The location of Strain 1 and Strain 2 in case of numerical model is shown in Fig. 6. The numerical model also showed the effectiveness of both inclined inserted as well as horizontally inserted reinforcing

bar in in-plane shear strength enhancement of masonry walls with openings. Stress concentration at the extreme edges of opening, causing diagonal shear cracking of URM specimen, was prevented for RM specimen with cracks distributed uniformly showing evenly distributed load sharing for RM specimen. It should be noted that noise for the strain gage data

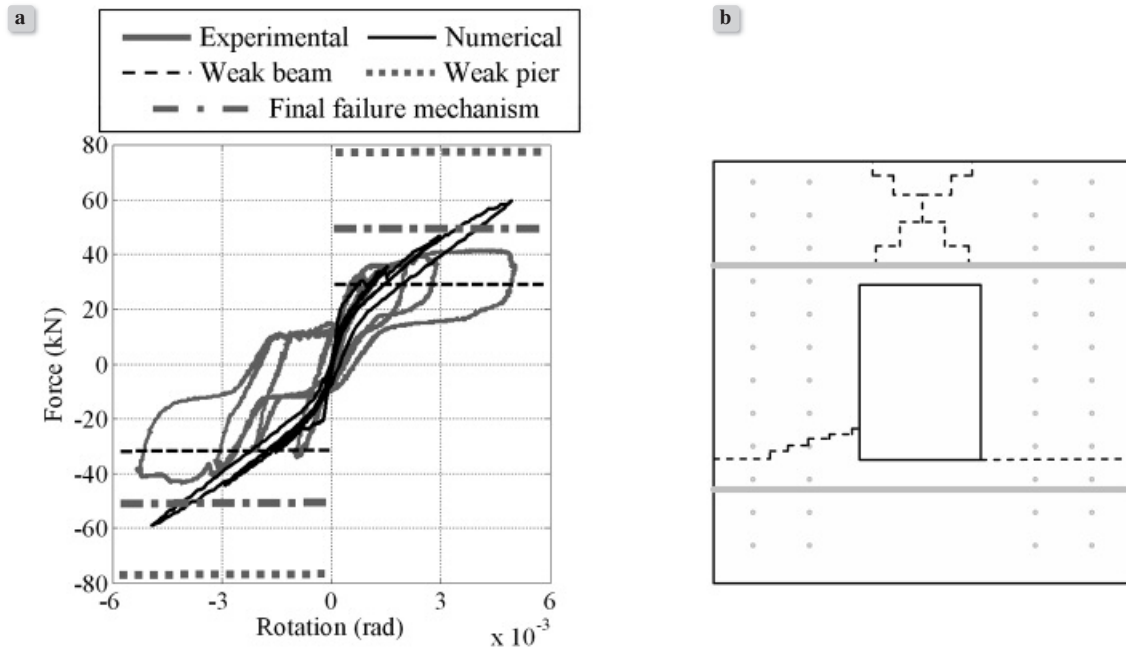


Figure 12.

Response for RM specimen for $\theta_{max} < 1/200$ radian: (a) Force deformation comparison; (b) Experimentally observed cracking pattern

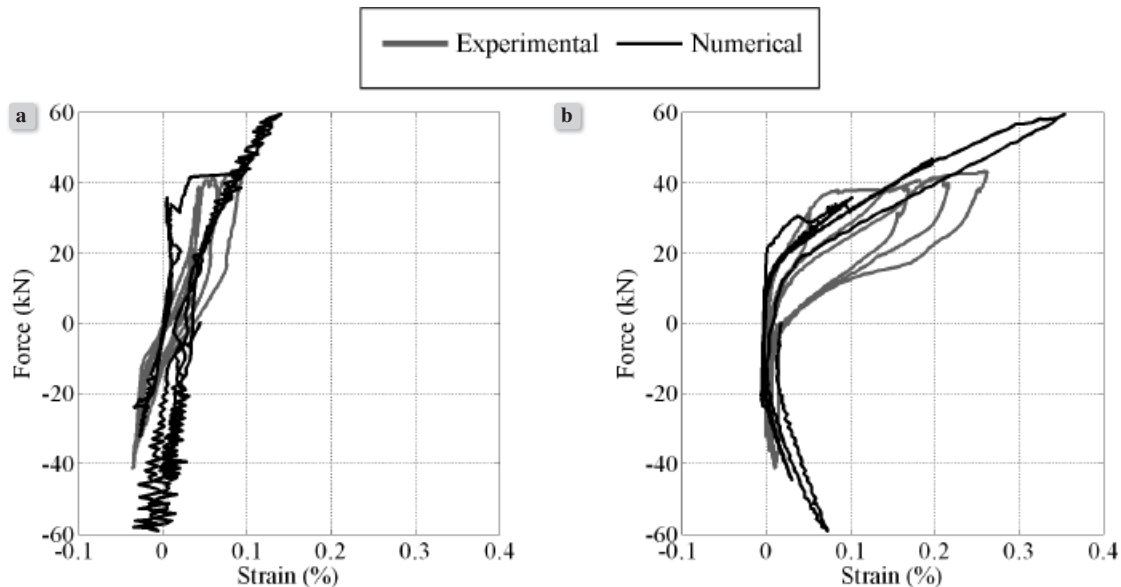


Figure 13.

Strain gage history comparison for RM specimen: (a) Strain 2; (b) Strain 1

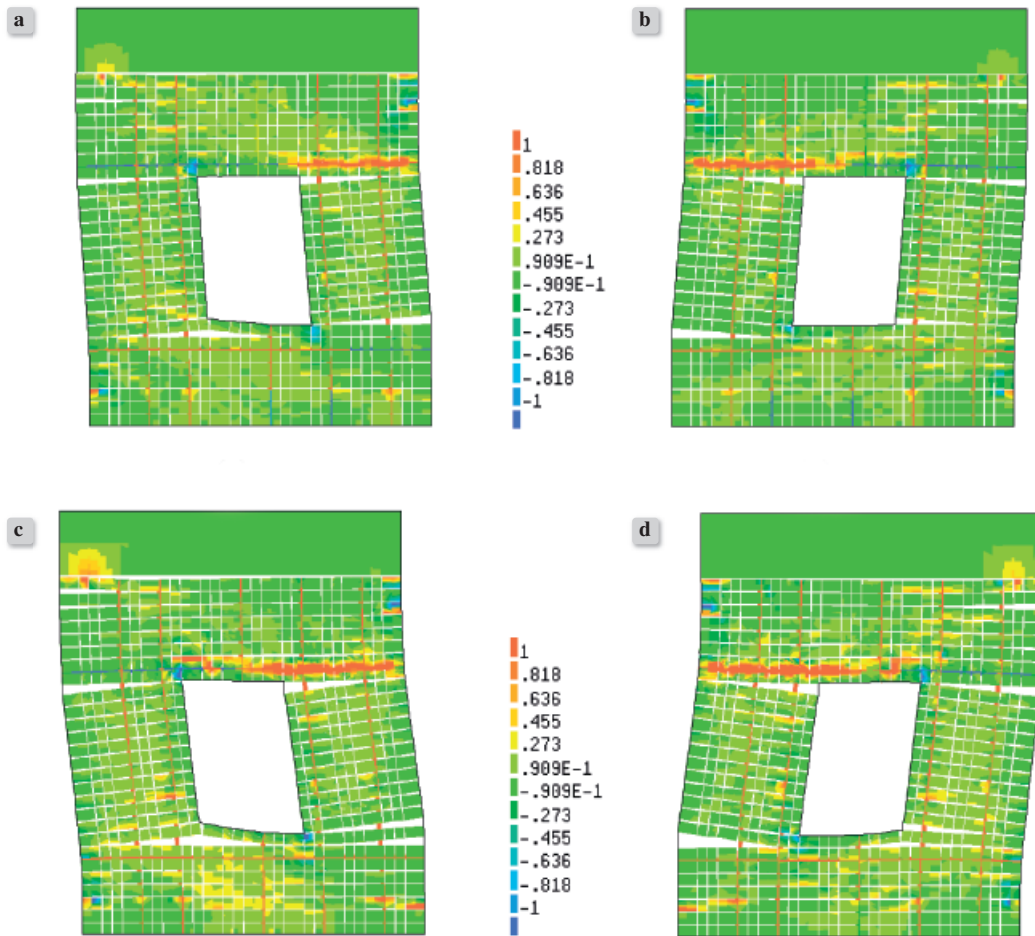


Figure 14. Deformed shape for RM specimen at: (a) $\theta_{max} = +0.003$ radian; (b) $\theta_{max} = -0.003$ radian; (c) $\theta_{max} = +0.005$ radian; (d) $\theta_{max} = -0.005$ radian (Deformation scale = 20)

obtained for Strain 2 persisted even at very small deformation load steps with maximum step size kept at 1/1000th of maximum deformation angle. The FE deformed shapes at different loading instants are shown in Fig. 14. The contour of colour in Fig. 14 represents the distribution of principal tensile and compressive stresses in FE model.

4.2.3. Comparison with theoretical predictions

As explained in Sections 3.1 and 3.2, theoretical predictions have been made assuming two extreme cases – strong pier-weak beam and strong beam-weak pier mechanisms. For strong pier-weak beam mechanism as shown in Fig. 8, using Eqn. 9 with $F_p (=16.66 \text{ kN})$ the strength of inclined inserted reinforcing bar, $L_{p1} (=330 \text{ mm})$, $L_{p2} (=550 \text{ mm})$, $L_{p3} (=110 \text{ mm})$, $L_{p4} (=440 \text{ mm})$ the distances of inclined inserted reinforcing bars from point of rotation, $w_d (=5.5 \text{ kN})$

the weight of pier, the calculated value of horizontal resisting force F_R^{URM} is 30.37 kN. The predicted strength slightly underestimates the resistance offered by masonry wall as shown in Fig. 12 (a).

Strong beam-weak pier mechanism assumes failure mechanism as shown in Fig. 9. Using Eqn. 13, the resisting force F_R^{URM} of 80.36 kN is obtained, which clearly overestimates the experimental response as shown in Fig. 12 (a). Here, $w_0 (=6.55 \text{ kN})$ and $w_d (=3.25 \text{ kN})$ are taken for computation. An additional plot has been made in Fig. 12 (a) with prediction based on the final failure pattern and subsequent formulation as given in Appendix Section B1. The resisting force computed from final failure mechanism gives value of 49.9 kN which agrees well with the ultimate resisting force observed as discussed in Section B1 of Appendix.

5. DISCUSSION

Both the experimental observations and numerical simulations showed effectiveness of the pinning retrofitting technique for in-plane shear loaded masonry walls. Retrofitted masonry walls showed sufficient strength enhancement that can avoid brittle collapse during earthquake excitation. Large variations in masonry mechanical properties can be found in historical masonry structures; therefore this becomes highly important when selecting the retrofitting technique in actual practice. Sensitivity studies performed on the pinning-retrofitted specimens [9] showed that variations in mechanical properties of masonry materials do not significantly affect post cracking response of the specimens, demonstrating the robustness of the proposed retrofitting technique.

It should be noted that choice of epoxy resin as bonding agent is mainly governed by its superior workability over ordinary cement pastes. The use of highly stiff epoxy resin in very deformable masonry would cause unexpected cracks when under high compressive stresses; however, present study involves study on in-plane shear behavior with moderately low level of compressive stresses. Furthermore, authors have also been involved in development of polymer-cement pastes in place of epoxy resin as a better choice from this point of view [20].

The resisting force computed for FE results and theoretical predictions matched well with each other. The FE result was moderately located between the two extreme theoretical estimations of weak beam and weak pier. Comparison of results for experimental observation and numerical simulation showed that FE prediction slightly overestimated the resisting force value. Bond slip of reinforcing bar might have influenced the failure mechanism during the tests, however, numerically developed model assumed a perfect bond between the reinforcing bars and masonry elements. This could be one of the reasons for overestimation of strength by numerical models. Failure pattern observed experimentally for RM specimen was wide spread with extensive cracking at the top mortar joint between the top steel beam and wall specimen. The top portion of specimen underwent significant damage as shown in Appendix Section B1 with rocking of piers representing mix failure mechanism which neither belonged to weak beam nor weak pier mode of failure as discussed in Section 3. FE simulation for similar test set-up did show wide cracks at the top mortar joint similar to experimental observation but the response was largely dominated by failure mechanism closer to weak

pier mode of failure with relatively stronger upper portion. This could also have resulted in overestimation of the resisting force. Hence, numerical model is particularly applicable for specific case of perfect bond between reinforcing bars and masonry elements. Nevertheless, the numerical results, with sufficient exactness, provided a strong basis for strength prediction as well as defining possible locations of stress concentrations and stated the effectiveness of retrofitted specimen with both inclined and horizontally inserted reinforcing bars. In a modified calculation for application in practice, such bond strength would be taken with some decreasing factor.

6. CONCLUSION

This paper has presented a 2D FE modelling scheme and theoretical prediction formulation for assessing the nonlinear load-deformation behaviour and failure mechanism of masonry walls reinforced by inserting inclined and horizontal steel bars when subjected to cyclic in-plane shear loading. FE models have been generated with simplified micro-modelling strategy, where bricks, mortar joints and reinforcing bars are represented by continuum elements, interface elements, and truss elements, respectively. A simplified FE model with equivalent vertical bars representing inclined inserted bars has been proposed. This concept of equivalent vertical bar allows simple theoretical prediction of wall strengths and makes a 2D FE modelling possible for the particular retrofitting technique. The FE model showed comparable results with the experimental observations with good agreements on strain gage histories. The experimental and numerical results demonstrate the effectiveness of the present retrofitting technique under cyclic loading conditions with enhancement in strength as well as ductility as compared to unreinforced specimen.

ACKNOWLEDGEMENTS

This research was supported by Grant-in-Aid for Scientific Research (B) No. 20360253 and by the Kyoto University G-COE Program, both of which were provided by the Japan Society for the Promotion of Science (JSPS). We also thank for the support provided by Professor Sanae Fukumoto during experimental works. The comments and questions from the reviewer led to significant improvement of this paper. All the supports mentioned above are highly acknowledged.

REFERENCES

- [1] *Touliatos P. G.*; Seismic behaviour of traditionally-built constructions. Repair and Strengthening. In Petrini V. and Save M., editors, Protection of the architectural heritage against earthquakes, New York, Springer, 1996; p.57-69
- [2] *Modena C., Casarin F., Porto F. da, Munari M.*; LAquila 6th April 2009 Earthquake: Emergency and post-emergency activities on cultural heritage buildings. In Garevski M. and Ansal A., editors, Earthquake Engineering in Europe, New York, Springer, 2010; p.495-521
- [3] *Karantoni F. V., Fardis M.N.*; Effectiveness of seismic strengthening techniques for masonry buildings. Journal of Structural Engineering, ASCE, Vol.118, No.4, 1992; p.1884-1902
- [4] *ElGawady M. A., Lestuzzi P., Badoux M.*; A review of conventional seismic retrofitting techniques for URM. Proc. of 13th International Brick and Block Masonry Conference, Amsterdam, 2004
- [5] *Abrams D., Smith T., Lynch J., Franklin S.*; Effectiveness of rehabilitation on seismic behavior of masonry piers. Journal of Structural Engineering, ASCE, Vol.133, No.1, 2007; p.32-43
- [6] *Ehsani M. R., Saadatmanesh H., Velazquez-Dimas J. I.*; Behavior of retrofitted URM walls under simulated earthquake loading. Journal of Composites for Construction, Vol.3, No.3, 1999; p.134-142
- [7] *Willis C. R., Seracino R., Griffith M. C.*; Out-of-plane strength of brick masonry retrofitted with horizontal NSM CFRP strips. Engineering Structures, Vol.32, No.2, 2010; p.547-555
- [8] *Takiyama N., Nagae T., Maeda H., Kitamura M., Yoshida N., Araki Y.*; Cyclic out-of-plane flexural behaviour of masonry walls rehabilitated by inserting steel pins. Proc. Of the 14th WCEE, Beijing, 2008
Available at:
http://www.iitk.ac.in/nicee/wcee/article/14_S11-015.PDF
(Last accessed date: July 25, 2011)
- [9] *Shrestha K. C., Nagae T., Araki Y.*; Finite element modeling of cyclic out-of-plane response of masonry walls retrofitted by inserting inclined stainless steel bars. Journal of Disaster Research, Vol.6, No.1, 2011; p.36-43
- [10] *Yoshida N., Nagae T., Maeda H., Fukumoto S., Takiyama N., Shrestha K. C., Ibarada I., Araki Y.*; Cyclic in-plane shear-flexural experiments of masonry walls with opening reinforced by inserting stainless pins: Part I and II. Proc. of Annual Meeting of Architectural Institute of Japan, C-2:963-964, 2009; p.967-968 (In Japanese)
- [11] *Modena C., Valuzzi M. R., Tongini F. T., Binda L.*; Design choices and intervention techniques for repairing and strengthening of the Monza cathedral bell-tower. Construction and Building Materials, Vol.16, 2002; p.385-395
- [12] *Valuzzi M. R., Binda L., Modena C.*; Mechanical behaviour of historic masonry structures strengthened by bed joints structural repointing. Construction and Building Materials, Vol.19, 2005; p.63-73
- [13] *Schultz A.E., Hutchinson R.S., Cheok G.C.*; Seismic performance of masonry walls with bed joint reinforcement. Proc. of Structural Engineers World Congress, San Francisco, California, USA, 1998
- [14] *Gouveia J. P., Lourenco P. B.*; Masonry shear walls subjected to cyclic loading: Influence of confinement and horizontal reinforcement. Proc. Of tenth North American Masonry Conference, St. Louis, Missouri, USA, 2007
- [15] *Lourenco P.B., Rots J.G.*; Multisurface interface model for analysis of masonry structures. ASCE Journal of Engineering Mechanics, Vol.123, No.7, 1997; p.660-668
- [16] DIANA User's Manual Release 9.3, TNO DIANA BV, Delft, 2008
- [17] ASTM, Annual Book of ASTM Standards. Section Four, Construction, Volume 04.05, Chemical-Resistant Nonmetallic Materials; Vitrified Clay Pipe; Concrete Pipe; Fiber-Reinforced Cement Products; Mortars and Grouts; Masonry; Precast Concrete, ASTM International, West Conshohocken, PA, 2007
- [18] RILEM, RILEM Technical recommendations for the testing and use of construction materials, Taylor & Francis, New York, 1994
- [19] *Elshafie H., Hamid A., Nasr E.*; Strength and stiffness of masonry shear walls with openings. TMS Journal, Vol.20, No.1, 2002; p.49-60
- [20] *Shrestha K. C., Pareek S., and Araki Y.*; Use of polymer-cement pastes as bonding agents for pinning retrofitting of masonry construction. Proc. of Japan Concrete Institute, Vol.33 No.1, 2011; p.1661-1666

APPENDIX

A1. Large deformation range response for URM specimen

Fig. A1 shows experimentally observed large deformation range response for URM specimen. The force-deformation response clearly shows the rocking mechanism observed in URM specimen with increment in deformation load. The final failure pattern observed as shown in Fig. A2 (a) showed wide diagonal shear cracks with rocking of a single pier.

The horizontal resisting force of URM specimen is compared to the rocking resistance computed by the rigid-body assumption as shown in Fig. A2(b). From Fig. A2(b), equilibrium condition gives following expression:

Point A,
$$F_R = \frac{w_d L_d + (F_v + w_o) L}{H_f} \quad (A1)$$

L (=650 mm) is pier width, H_f (=1190 mm) the height of the reaction force from the point of rotation, w_d (=5 kN) the weight of the rocking pier, F_v (=20 kN) the load applied at the top of specimen, w_o (=4 kN) the weight of brick wall resting on the rocking pier, L_d (=303mm) the distance of centre of mass for rocking piers. The rocking capacity of URM specimen, F_R^{URM} calculated using Eqn. (A1) is 14.4 kN, plotted in Fig. A1 as final failure mechanism – the value is slightly lower compared to experimental observation. The reason for this difference is due to absence of shear strength parameter of masonry in Eqn. A1.

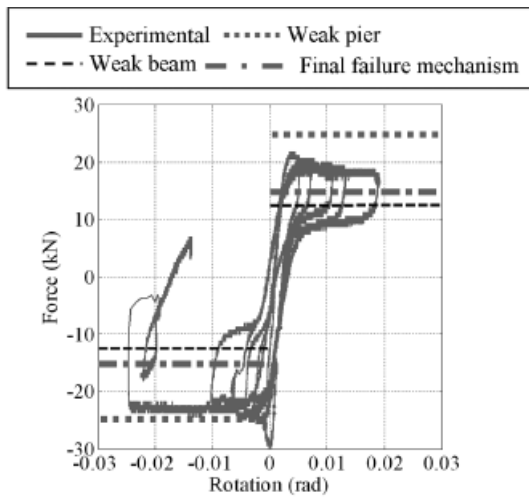


Figure A1. Force deformation comparison for URM specimen for $\theta_{max} < 1/50$ radian

B1. Large deformation range response for RM specimen

Fig. B1 (a) shows experimentally observed large deformation range response for RM specimen. The final failure pattern observed as shown in Fig. B1 (b) showed cracks evenly distributed in the wall with final failure mechanism showing rocking of piers. The rocking resistance computed using Eqns. 9 and 13 is plotted as dotted line in Fig. B1 (a). The results clearly show experimentally observed failure pattern and resisting force to lie in between the two extreme failure mechanisms assumed.

From Fig. B2, with mix failure mechanism representing the final cracking pattern observed experimentally, following equilibrium conditions for RM specimen can be obtained:

From free body T*:

$$F_R = F_A^H + F_B^H \quad (B1)$$

$$F_v = F_A^V + F_B^V$$

From free body A*:

$$F_A^H h_1 = F_A^V L_1 + w_d L / 2 + F_p^h h_2 + F_p L_2 + F_p (L_{p1} + L_{p2}) \quad (B2)$$

From free body B*:

$$F_B^H h_1 = F_B^V L + w_d L / 2 - F_p^h h_2 + F_p L_3 + F_p (L_{p3} + L_{p4}) \quad (B3)$$

Solving Eqns. B1, B2 and B3, the capacity of wall is obtained as follows:

$$F_R^{RM} = \frac{L}{h_1} \left\{ F_A^V \frac{L_1}{L} + F_B^V + w_d + F_p \frac{(L_2 + L_3 + L_{p1} + L_{p2} + L_{p3} + L_{p4})}{L} \right\} \quad (B4)$$

Here, L_2 (=930 mm), L_3 (=280 mm), w_d (=6 kN), h_1 (=1330 mm). Assuming $F_A^V = F_B^V = F_v / 2$, the rocking capacity of RM specimen, F_R^{URM} calculated using

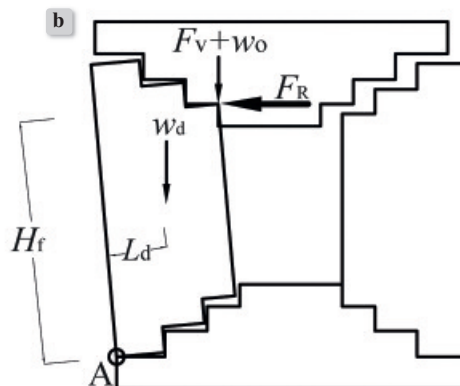


Figure A2. Final failure mechanisms for URM specimen: (a) Experimentally observed at $\theta_{max} = +0.02$ radian; (b) Theoretical prediction

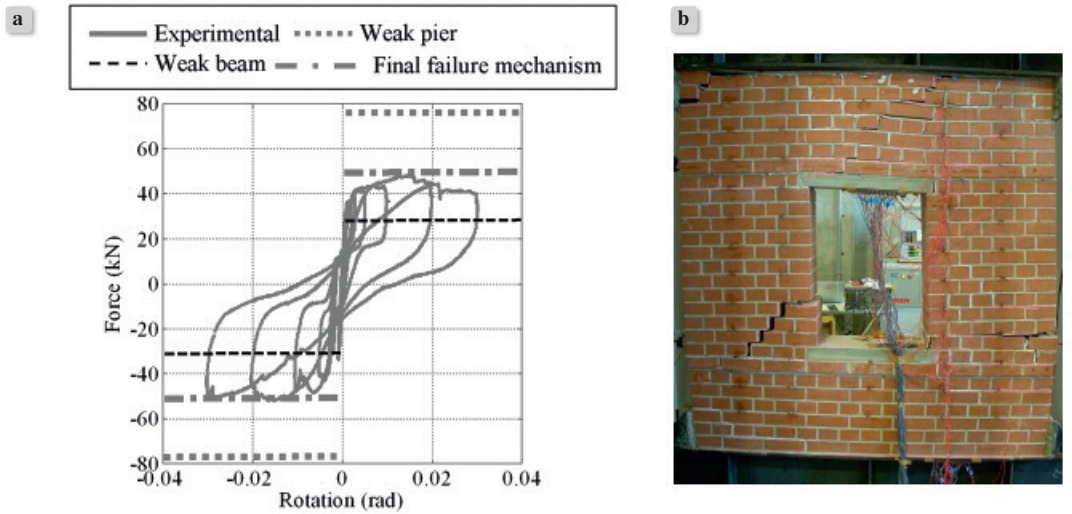


Figure B1. Response for RM specimen: (a) Force-deformation comparison; (b) Experimentally observed failure pattern at $\theta_{max} = +0.03$ radian

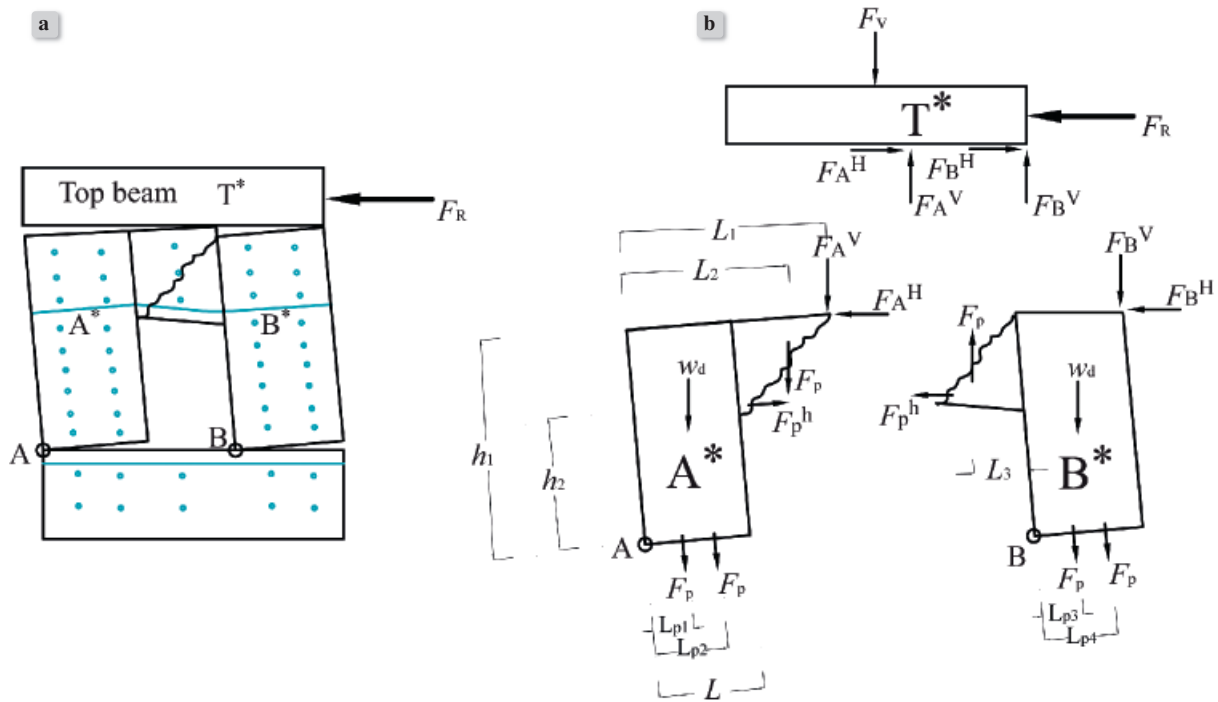


Figure B2. Experimentally observed final failure mechanism for RM specimen: (a) Deformed shape; (b) Free body diagrams

Eqn. (B4) is 49.9 kN. The result is plotted in Fig. B1(a) as final failure mechanism. The results show good prediction of the experimentally observed ultimate strength of RM specimen.